Sub-mesoscale Wind-Front Interactions: the combined impact of thermal and current feedback

Yue Bai [1], Andrew F. Thompson [1], Ana B. Villas Bôas[2], Patrice Klein[1,3], Hector S. Torres[3], Dimitris Menemenlis[3]

[1]California Institute of Technology
[2]Colorado School of Mines
[3]Jet Propulsion Laboratory

Key Points:

- Surface temperature gradients and vorticity anomalies at scales down to $O(10)$ km, impact wind stress curl and divergence jointly.
- Wind-front interactions at submesoscales are at least an order of magnitude stronger than at mesoscales.
- Reconstruction of the wind stress curl using both thermal and current feedback is 10-40% more accurate than relying on a single feedback.

Corresponding author: Yue Bai, ybbai@caltech.edu

Abstract

Surface ocean temperature and velocity anomalies at meso- and sub-meso-scales induce wind stress anomalies. These wind-front interactions, referred to as thermal (TFB) and current (CFB) feedbacks, respectively, have been studied in isolation at mesoscale, yet they have rarely been considered in tandem. Here, we assess the combined influence of TFB and CFB and their relative impact on surface wind stress derivatives. Analyses are based on output from two regions of the Southern Ocean in a 4-6 km-resolution coupled simulation. Considering both TFB and CFB shows regimes of interference, which remain mostly linear down to the simulation resolution. The jointly-generated wind stress curl anomalies approach 10^{-5} Nm^{-3}, $\sim$20 times stronger than at mesoscale. The synergy of both feedbacks improves the ability to reconstruct wind stress curl magnitude and structure from both surface vorticity and SST gradients by 12-37% on average, compared with using either one alone.

Plain Language Summary

Surface ocean temperature and velocity anomalies at 0.1-100 km scales imprint their signatures on the surface wind stress, which in turn supplies the ocean with momentum. This process is called wind-front interaction and typically referred to as thermal (TFB, by temperature gradients) and current (CFB, by velocity gradients) feedbacks. Previously, studies using satellite observations and regional numerical models have studied either feedback in isolation. However, consideration of both in tandem remains immature. Here, we present an approach that assesses both feedbacks' combined and relative impact on the surface wind stress. We rely on output from an air-sea coupled simulation at 4-6 km ocean resolution. This approach allows us to identify constructive and destructive patterns of how the two feedbacks interact, which remain mostly linear down to the simulation resolution. The jointly-generated wind stress derivative anomalies are 20 times stronger than observed previously at larger scales. Considering both feedbacks, reconstructions of wind stress derivatives are viable and have 10-40% less error on average compared with using either feedback by itself. Contributions from either feedback in modifying wind stress fields vary temporally and can be related to physical properties such as surface wind speed and air-sea temperature difference across the studied area.

1 Introduction

The exchange of heat and momentum between the ocean and the atmosphere is a critical component of global climate evolution. Processes that govern air-sea coupling and the transfer of climate-relevant tracers occur across a broad range of scales (Small et al., 2019; Strobach et al., 2022; Renault et al., 2018; Chang et al., 2020; Seo et al., 2023), with transitions in air-sea behavior occurring at a few key spatial scales. At the basin scale, the atmosphere supplies the momentum that powers the ocean currents (Rai et al., 2021) and determines the oceanic distribution of latent and sensible heat fluxes (Small et al., 2008, 2019). At oceanic mesoscale, or spatial scales of $O(100)$ km and Rossby number $\mathrm{Ro} = \zeta/f \ll 1$, these relationships reverse and ocean surface variability triggers atmospheric responses (Chelton & Xie, 2010; Renault et al., 2016; Small et al., 2019; Frenger et al., 2013; Seo et al., 2023). This change in behavior occurs due to two dynamical processes that become relevant at the scale of ocean mesoscale eddies: the thermal and current feedbacks (TFB and CFB), which are related to surface ocean temperature and velocity gradients, respectively. Wind-front interactions have been studied almost exclusively using satellite products (e.g., Chelton et al., 2004) and mesoscale-resolving numerical simulations. In the ocean, however, another dynamical transition occurs at $O(10)$ km, scales smaller than the mesoscale, where the Rossby number approaches $O(1)$. While the impact of these smaller, sub-mesoscale ($O(10)$ km) features on air-sea interactions remains largely unconstrained, they are characterized by strong anomalies in vorticity and

density gradients (Siegelman et al., 2020; Taylor & Thompson, 2023; Balwada et al., 2018) that may contribute to the TFB and CFB.

The thermal component of wind-front interactions assesses the "bottom-up" (Renault et al., 2018) thermodynamic influence of sea surface temperature (SST) gradients on the atmospheric wind fields and atmospheric boundary layer above (Chelton et al., 2004). Forerunner studies, such as Chelton et al. (2001, 2004); O'Neill et al. (2012), empirically established positive linear relationships between wind stress divergence and wind stress curl with downwind and crosswind SST gradients (defined in Sec. 3.1), respectively. Mechanisms that support the TFB coupling were reviewed in detail by Small et al. (2008). Gradients in SST modify the overlying atmospheric boundary layer stability and the surface drag coefficient. This in turn generates mesoscale variability in wind speed and stress through either pressure adjustment or downward momentum transfer (Frenger et al., 2013; Desbiolles et al., 2023). Chelton et al. (2007, 2011); O'Neill et al. (2012) quantified these correlations through linear coupling coefficients and found seasonal fluctuations in the coupling intensity (Chelton & Xie, 2010). The TFB influences the distribution of latent and sensible heat fluxes (Foussard et al., 2019), and induces wind stress curl anomalies that can enhance Ekman pumping, especially in the Southern Ocean (Gaube et al., 2015).

Current feedback (CFB), the mechanical driver of wind-front interactions, arises from the difference between surface vector winds and surface ocean currents. Since mesoscale eddies are typically of smaller spatial scale than atmospheric variations, the air-sea velocity difference is non-uniform across the eddy. This feature causes eddies with positive vorticity to generate a negative wind stress curl anomaly (Renault et al., 2016). Bye (1985); Rooth and Xie (1992) showed analytically that the negative correlation between vorticity and wind stress curl is linearly dependent on the magnitude of the local surface wind speed. Renault et al. (2017) used mesoscale satellite observations to confirm that the current-stress coupling coefficient depends on local surface wind speed. CFB is a sink of the oceanic mesoscale geostrophic kinetic energy to the atmosphere (Renault et al., 2016; Xu & Scott, 2008). This "eddy killing" effect acts through the wind stress curl-induced Ekman pumping (Gaube et al., 2015) that counteracts the eddy vorticity and therefore weakens the eddies (Renault et al., 2018). At mesoscales, where flows are to leading order geostrophic and divergence-free, the connection between surface current divergence and wind stress divergence is often neglected (Renault et al., 2018).

Recent high-resolution numerical simulations have enabled a first exploration of sub-mesoscale wind-front feedbacks, and provide evidence that they are significantly enhanced. Strobach et al. (2022) focused on SST fronts of $\sim$10 km in the Gulf Stream using a sub-mesoscale-resolving coupled simulation. Mesoscale frontogenesis gives rise to SST gradients that are up to 20 times stronger than those observed in pioneering mesoscale studies (e.g., Chelton et al., 2004). These sub-mesoscale SST gradients generate large wind stress curl anomalies up to 10^{-5} Nm^{-3} and intermittent periods of strong latent heat flux of 300 W m^{-2}. In an idealized simulation, Chen et al. (2022) confirmed the enhancement of CFB due to sub-mesoscale surface vorticity anomalies that exceed the local Coriolis parameter f. At the sub-mesoscale, flow begins to escape the constraint of Earth's rotation, and surface divergence starts to assume a comparable magnitude as the surface vorticity (Thomas et al., 2008; McWilliams, 2016; Callies et al., 2020). At those small spatial scales, a negative linear correlation between surface divergence and wind stress divergence was recently identified (Chen et al., 2022), in addition to the well-established correlation between ocean vorticity and wind stress curl. The impact of sub-mesoscale wind-front interactions on globally-integrated heat and momentum budgets are yet to be quantified.

Most previous studies, including recent studies that resolve sub-mesoscales, quantify wind stress derivatives as a function of either TFB or CFB, but rarely consider the two processes in tandem. Chelton et al. (2004) pointed out that strong density fronts are often collocated with strong currents and speculated that wind stress curl modifi-

cations from TFB could potentially be contaminated with CFB (Small et al., 2008). Renault et al. (2019) and Takatama and Schneider (2017) developed controlled mesoscale simulations to separate the two feedback mechanisms by only having one active at a given time, and identified their individual contribution to wind stress curl. However, in a coupled simulation or using observations, it is not possible to separate the impact on the wind stress derivatives from individual feedback mechanisms, and predictions from these "1D" studies, hereby referred to as 1D current or 1D thermal analysis, may be inaccurate due to the combination or cancellation of correlated TFB and CFB. In this study, we use output from a high-resolution coupled climate model to show that there is a large region of parameter space, where an accurate prediction of wind stress derivatives requires, accounting for both feedbacks. We adopt a "2D" perspective that incorporates both TFB and CFB and assesses their joint influence and relative importance simultaneously.

2 Methods and Study Region

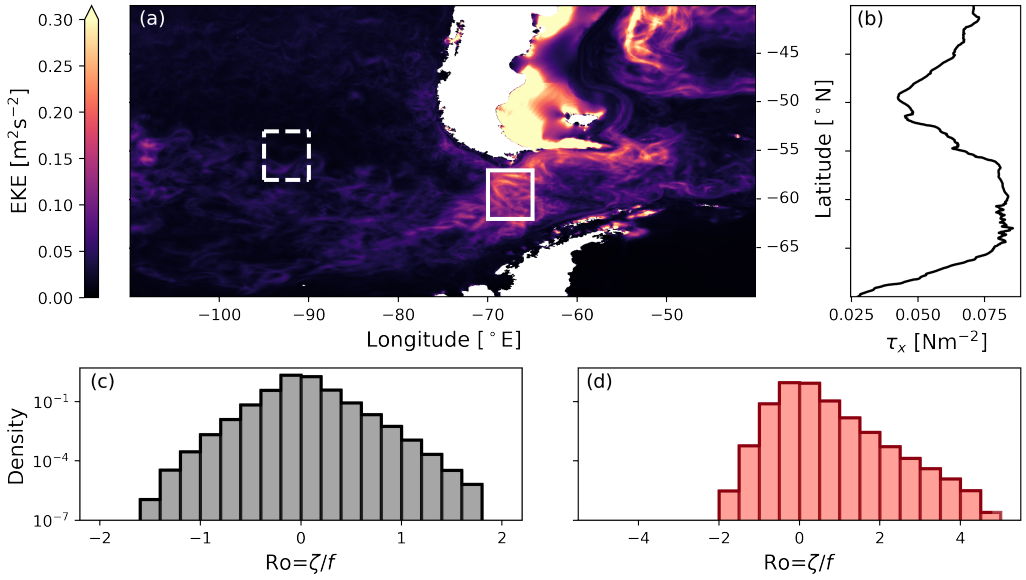

Figure 1. Southern Ocean study domains. (a) Mean surface eddy kinetic energy (EKE [m^2 s^{-2}]) for austral winter months in 2012, taken from the COAS simulation (see section 2), for the Pacific sector of the Southern Ocean. The white boxes show two subdomains that are the focus of this study. The western (dashed) and eastern (solid) boxes correspond to quiescent (58-53°S, 95-90°E) and energetic (62-57°S, 70-65°E) regions, respectively. (b) Zonally-integrated zonal wind stress for the region shown in panel (a). (c) Histogram of Rossby number in the quiescent region; (d) histogram of Rossby number in the energetic region.

In this study, we use outputs from the state-of-the-art global Coupled Ocean-Atmosphere Simulation (COAS), or commonly referred to as C1440-LLC2160. The oceanic component of COAS has a horizontal grid spacing of 1/24°, rounding to ∼2 km around Antarctica. The atmospheric models has a nominal horizontal grid spacing of 6.9 km. Information exchange between them happens every 45 seconds. The simulation was initialized on January 20th, 2012 and results shown below are based on output from June 1st to August 31st, 2012 (JJA). This configuration is identical to that used in Torres et al. (2022), from which the readers can find more general information on the model and ex-

periment setup. The unprecedented spatial and temporal resolutions of this global coupled simulation make it a unique and necessary tool to study meso-to-sub-mesoscale wind-front interactions, a regime that remains under-explored.

The present study focuses on two subdomains that are within or close to the Drake Passage region of the Southern Ocean (Fig. 1), where the impact of variable ocean surface properties is disproportionally large (Nicholson et al., 2022). We select this region because it experiences the wind stress maximum (Fig. 1 b) and the Southern Ocean is the principal site of surface and deep water exchange and ventilation (Marshall & Speer, 2012; Dove et al., 2021; Gruber et al., 2019), which might be impacted by vertical velocities induced by additional wind stress curl from wind-front interactions (Gaube et al., 2015; Renault et al., 2023). Furthermore, the two $5°\times5°$ subdomains compare a quiescent, low eddy kinetic energy (EKE) regime, and a turbulent frontal region with higher background energy levels, the latter of which have been shown to localize ventilation enhancement (Dove et al., 2022, 2023). Surface Ro distribution (Fig. 1c,d) for quiescent and energetic regions both favor cyclonic eddies and respectively have skewness values of 0.4 and 0.9, suggesting more sub-mesoscale fronts (Buckingham et al., 2016; Barkan et al., 2019) and frontal slumping (Hoskins & Brertherton, 1972) in the energetic region. In the following sections, we highlight the 2D approach and the synergy of thermal and current feedbacks with output from the energetic region. These results are then compared with those from the quiescent subdomain in the Supplementary Information (SI) to show preliminary regional variations. A more thorough regional and temporal analysis of wind-front interactions is beyond the scope of this study and left for future work.

3 Results

In this section, we consider the relative importance of both TFB and CFB by constructing a series of two-dimensional, binned-averaged, conditional mean plots that evaluate the joint dependence of wind stress curl and divergence on surface ocean vorticity/divergence and temperature gradients. We also quantify the relative contribution of each feedback on wind stress properties via linear coefficients, and investigate the temporal variability of these coefficients as well as the mechanisms that give rise to the variability.

3.1 Combined impact of thermal and current feedbacks

The dependence of wind stress curl and divergence on surface ocean properties illustrates scenarios and regimes where, if considered using the 2D approach, CFB and TFB combine constructively and destructively. These regimes are evaluated by bin-averaging the hourly wind stress curl or divergence as a function of two properties, one chosen from each category: ocean vorticity and divergence, or crosswind and downwind SST gradient. Crosswind SST gradients are defined by $\boldsymbol{\nabla} SST \times \boldsymbol{\tau}$ in which the winds are aligned with the front. In downwind SST gradients, $\boldsymbol{\nabla} SST \cdot \boldsymbol{\tau}$, the winds are perpendicular to the frontal direction. Ocean vorticity and divergence are normalized by the absolute value of f, while SST gradients are scaled by a typical sub-mesoscale frontal length scale, $\sim$ 10 km. Note that the normalizations are different from previous mesoscale studies in order to highlight sub-mesoscale features. A series of conditional mean plots (Fig. 2) are constructed with non-uniform bin sizes as data points are sparse for extreme values; non-dimensionalized vorticity ($\zeta/|f|$) and divergence ($\delta/|f|$) have bin sizes ranging from 0.1 near 0 to up to 0.5 at ±4; crosswind and downwind SST gradient bin sizes range from $0.1°$C/10 km near 0 to $0.4°$C/10 km at ±8. The results discussed below are qualitatively similar for uniform bin sizes. We calculate the mean and other statistical moments like standard deviations using hourly output, to which we applied a one-day running mean to each field to remove high-frequency variability, likely related to atmospheric fluctuations. Specifically, all values of wind stress curl/divergence over the full austral winter period (JJA, 2012) are collected for a given combination of vorticity/divergence and

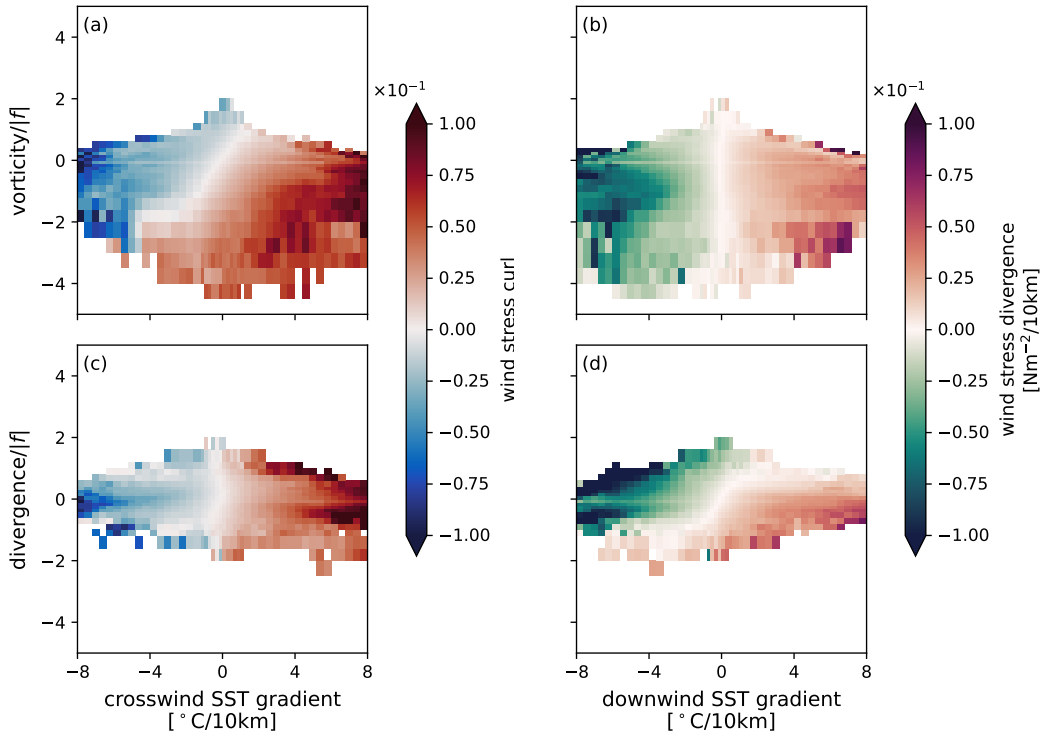

Figure 2. Conditional mean plots conditioned on surface ocean vorticity or divergence and crosswind or downwind SST gradients, colored by mean values of either wind stress curl or wind stress divergence. (a) The joint influence of vorticity and crosswind SST gradient on wind stress curl. (b) TFB from downwind SST gradient on wind stress divergence. (c) TFB from crosswind SST gradient on wind stress curl. (d) The joint influence of ocean divergence and downwind SST gradient on wind stress divergence. The slope of the zero-line (white in both colormaps) indicates the level of interaction and competition between surface vorticity/divergence and cross-wind/downwind SST gradients in generating small-scale features in the wind stress fields.

crosswind/downwind SST gradient, from which the standard deviation is first calculated. Data that exceed ±1 standard deviation, in each bin combination, are removed before computing the mean wind stress product to further minimize outliers introduced by synoptic events. The following analyses on slopes and coefficient calculation in Sec. 3.2 are not sensitive to this standard deviation cutoff.

There are eight possible combinations from two sets of surface variables as axes (ocean vorticity/divergence and cross/down-wind SST gradients): four for wind stress curl and four for wind stress divergence. Four are highlighted in Fig. 2 that are representative of different CFB and TFB regimes. When only one property is relevant to the wind stress derivative, the conditional mean plot provides similar information as the independent 1D approach; when both properties are correlated with the wind stress field, the 2D perspective show patterns of interaction.

Between the two chosen axes of the conditional mean plot, if only one of the properties is contributing actively to wind-ocean feedbacks, then the wind stress derivative only varies along a single axis, e.g. Fig. 2 b and c. This essentially reduces to an independent 1D analysis. In Fig. 2b, the mean wind stress divergence is close to zero when the downwind SST gradient is weak, for all possible values of vorticity. Positive down-

wind SST gradients lead to a positive wind stress divergence. This indicates that SST gradients and the TFB dominate small-scale structures in wind stress divergence, while surface vorticity plays a negligible role in setting small-scale variability. By averaging across surface vorticity values, the traditional 1D binned analysis of the TFB slope compares well with previous studies (e.g., Chelton & Xie, 2010). TFB also occurs where crosswind SST gradient is positively correlated with wind stress curl, while ocean divergence, as the other axis, has a limited impact (Fig. 2c).

The conditional mean analysis also illustrates regimes where components from both CFB and TFB contribute to wind stress gradients. In Fig. 2a, both vorticity and crosswind SST gradients shape small-scale variations in wind stress curl. For a given surface vorticity, wind stress curl increases linearly with crosswind SST gradient. However, meso- and smaller-scale features in wind stress curl are at the same time imprinted from surface ocean vorticity, which causes wind stress curl to decrease with increasing vorticity, at fixed crosswind SST gradients. Together, this causes the zero-line (white) in wind stress curl to be tilted and maintained between the independent TFB- and CFB-dominant regimes. CFB constructively reinforces TFB feedback in the second (negative SST gradient and positive vorticity) and fourth (positive SST gradient and negative vorticity) quadrants, while destructively attenuating or even reversing the sign of the wind stress curl anomaly in the first (positive SST gradient and vorticity) and third (negative SST gradient and vorticity) quadrants. The combined influence is also present in Fig. 2d, in which wind stress divergence is a function of both ocean surface divergence and downwind SST gradients. The constructive interaction between both feedbacks suggests that anomalously large wind stress curl or divergence occurs at large magnitudes of SST gradients and surface vorticity or divergence values, when they have the opposite signs. In Fig. 2 a, the jointly-generated wind stress curl approaches anomalously positive values that are over 0.1 Nm^{-2}/10 km, about 20 times stronger than in previous mesoscale studies (e.g., Chelton et al., 2004). This enhancement at small scales is also consistent with Strobach et al. (2022)'s 1D study on submesoscale thermal feedback. These results also confirm in a realistic numerical setting that strong submesoscale surface ocean divergence imprints on wind stress divergence, first shown in an idealized simulation by Chen et al. (2022). Although high-resolution 1D studies show enhanced feedback impact, they neglect variations from the other feedback and tend to underestimate wind stress curl or divergence, which is illustrated in Sec. 3.2.

3.2 Vorticity and crosswind SST gradient: contribution and variability

Based on the interaction between both feedbacks, in this section, we test the hypothesis that most variance in wind stress fields can be explained by a combination of ocean surface vorticity/divergence and cross/downwind SST gradients when the wind stress field is not dominated by synoptic events. The following analysis is focused on the dependence of wind stress curl on surface vorticity and crosswind SST gradients, but the same idea applies to wind stress divergence (see SI). Following the 2D approach, we propose a dependent, bivariate, as opposed to univariate, and linear model to reconstruct wind stress curl:

$$\boldsymbol{\nabla} \times \boldsymbol{\tau} = \alpha \, \boldsymbol{\zeta}/|f| + \beta \, \boldsymbol{\nabla}_c \mathrm{SST}, \tag{1}$$

where coefficients α and β are solved simultaneously by inverting the matrix whose columns correspond to vorticity scaled by $|f|$ and crosswind SST gradients scaled by 10 km within the subdomain and over the desired time scales. Note that the coefficients vary with the chosen normalization, but the relative contributions of the two terms on the right-hand side of (1) are not dependent on normalizations. These coefficients are directly related to the 2D wind stress curl distributions, such that the ratio of α and β corresponds to the zero-line slope (not shown) in Fig. 2a. To assess the dependence of TFB and CFB, we compare this 2D dependent reconstruction to 1D current + thermal reconstruction.

For the latter case, linear coefficients that determine how wind stress curl depends on CFB and TFB are solved independently and then applied to (1), i.e. the inferred "1D" contributions are summed. To illustrate the importance of including both feedbacks on wind-front interactions, reconstructions based on just 1D current ($\beta = 0$) or 1D thermal ($\alpha = 0$) feedback are also computed for comparison.

Among the various reconstruction approaches, the ones that incorporate both feedbacks (2D and 1D current + thermal) provide a more accurate representation of the variance of wind stress curl (Fig. 3). We solve for the 2D and 1D coefficients at hourly intervals in the energetic subdomain (Fig. 1) and reconstruct the wind stress curl linearly based on (1). Notably, from the bivariate 2D and 1D current + thermal approaches (Fig. 3 b,e and g,j), the reconstructed wind stress curl has similar magnitudes. By comparison, univariate reconstruction performances based on one feedback, 1D current (Fig. 3 c,h) or 1D thermal (Fig. 3 d,i), fluctuate in time and suggest that CFB or TFB dominance can vary even in a localized region. To statistically quantify their agreement with the simulated wind stress curl, for each method, the hourly Pearson correlation coefficient squared r^2 is shown in Fig. 3k. Agreement between the two time series of r^2 reconstructed by both feedback suggests similar spatial structures, while 1D current or 1D thermal feedback preferably recovers vorticity or filamentary structures, respectively. The r^2 values indicate that skill in reconstructing wind stress curl improves when both feedbacks are involved. Specifically, the 1D current and 1D thermal reconstructions have 40% and 10% larger domain-averarged root-mean-square error (RMSE) for the three-month period (Fig. 3 l) than the 2D reconstruction. The 1D independent sum slightly under-performs the 2D approach, with 3% more RMSE. However, caution should be taken in interpreting the reconstruction performance, as (1) is limited when large-scale wind stress curl anomalies pass through the subdomain, potentially linked to synoptic events, as discussed in Sec. 4.

The 2D coefficients improve the wind stress curl reconstruction, but their values are time dependent (Fig. 4). α and β are calculated as in (1) with one-, five-, and fifteen-day time windows within the energetic domain. For each case, the coefficients are calculated by updating the center of the window by one day; the values are plotted at the window midpoint in Fig. 4 b,c. Wintertime daily-calculated α has a mean of -0.017±0.006 N m^{-2}/10 km and β has 0.013±0.007N m^{-2}/°C. The standard deviation for both reduces to ~ 0.003 at 15-day time scale. The ratio, $\beta/|\alpha|$, across all three windowing time scales is about 0.8 10km/°C, which is consistent with the zero-line slope in Fig. 2 a.

We explored a wide range of physical properties at the air-sea interface that could contribute to variations in α and β, and find that the most relevant are wind speed and air-sea temperature difference, respectively (Fig. 4 a,d). Within one-, five-, and fifteen-day time windows, wind speed at 10 m and each coefficient are scattered and the correlation between them is quantified with Pearson linear coefficients r_{W_α} and r_{W_β} (Fig. 4 e,f). Absolute values of r_{W_α} and r_{W_β} both increase with windowing length. Having $r_{W_\alpha} > 0.8$ indicates that α has a tight linear correlation with wind speed; this is weaker between β and wind speed with r_{W_β} ranging from 0.6-0.8. Indeed, 1D binned averages of wind speed, with bin sizes 1 m s^{-1}, and standard deviation within each bin are calculated, and β has a spread that is twice as large compared with α, on average. We then explore β's relationship with air-sea temperature difference, noting that the quadratic drag coefficient of wind stress calculation, C_d, depends on this temperature difference. The correlation, r_{T_β}, ranges from $0.4-0.7$, with the largest r_{T_β} occurring for one-day time windows. The implications of the correlation dependence on time scale are discussed in Sec. 4.

4 Discussion

This study emphasizes the importance of a 2D perspective on wind-front interactions at sub-mesoscales that accounts for the joint impact from TFB and CFB. This is

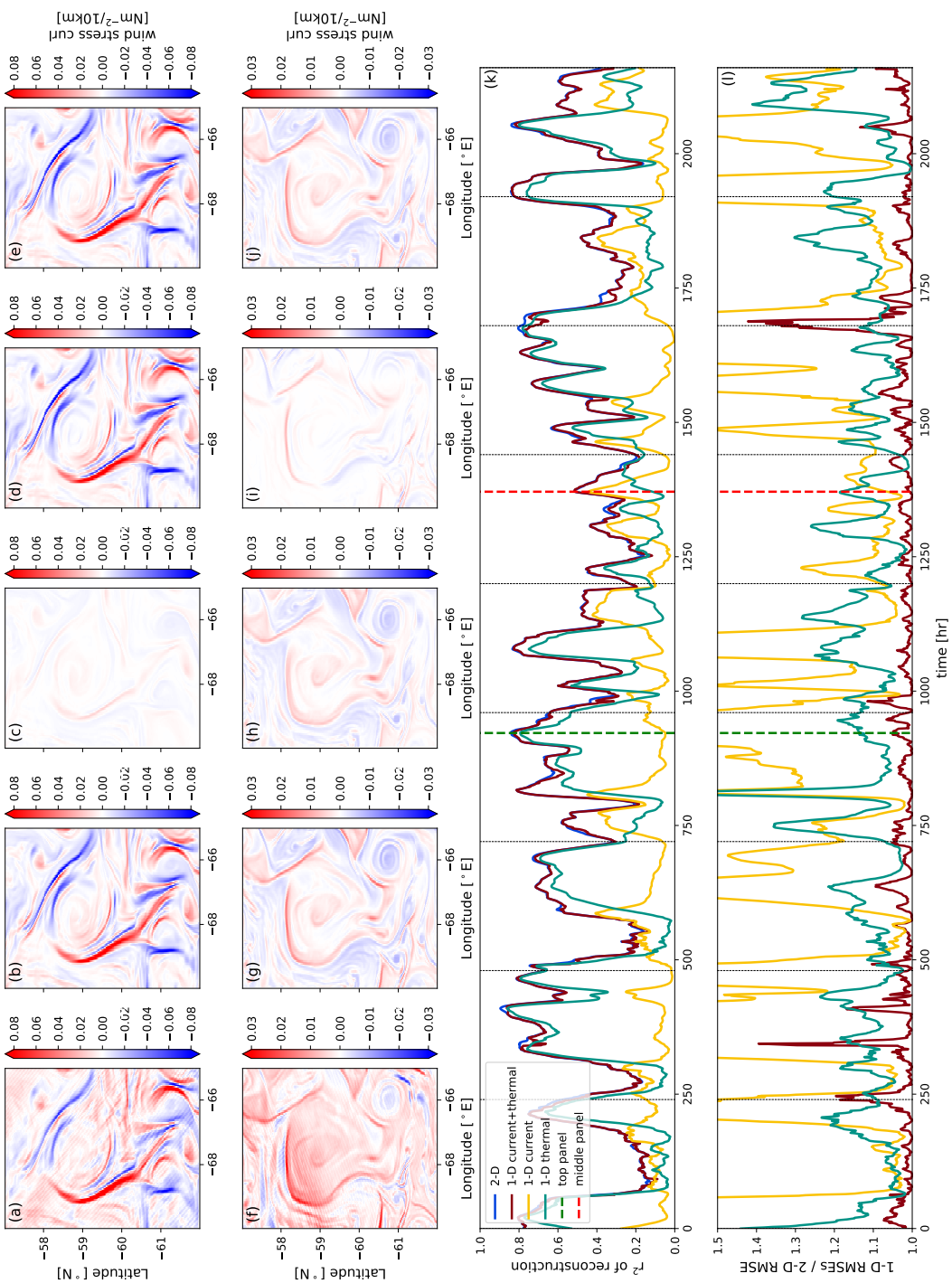

Figure 3. Illustration of reconstruction performances with simulated wind stress curl snapshots and hourly reconstruction variability. Within the top two panels (a-j), from left to right, each columns are: (a,f) wind stress curl directly from the numerical simulation, (b,g) wind stress curl estimated by 2D dependent coefficients for current and thermal feedback, (c,h) reconstruction based on 1D current feedback, (d,i) reconstruction based on 1D thermal feedback, (e,j) followed by reconstruction from 1D current + thermal independent sum. Pearson linear correlation coefficients squared (r^2) of each reconstruction and simulated wind stress curl are calculated per hour in (k). The root-mean square error of all 1-D reconstruction methods against the 2-D one are averaged through the subdomain in (l). One instance each of thermal and current feedback dominance are indicated by the dashed lines and correspond to snapshots (a-e) and (f-j), respectively. Black dashed lines separate every 10 days.

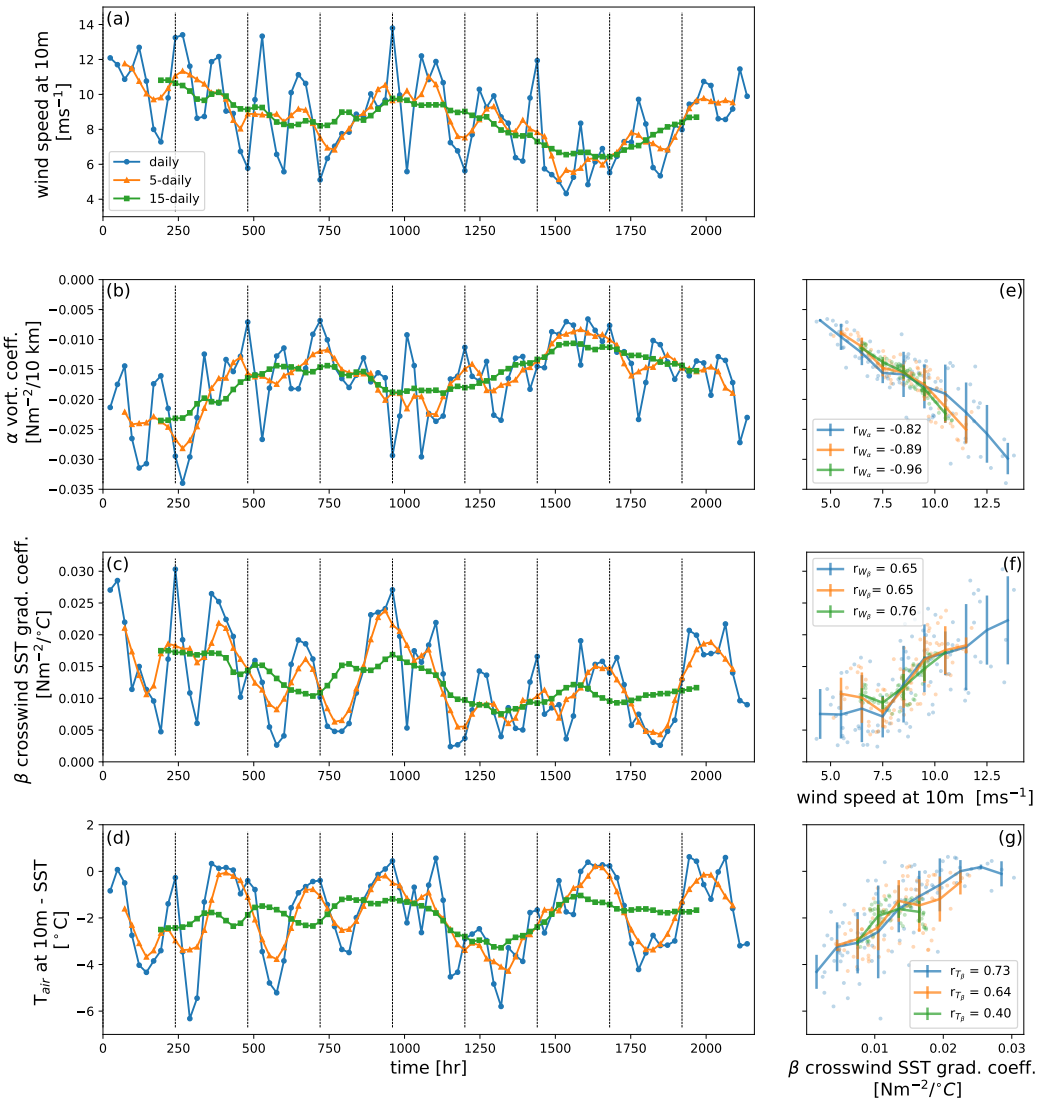

Figure 4. Variability and correlation of coefficients, α and β, and related physical properties, wind speed and air-sea temperature difference. (b) α; (c) β. (a) Wind speed and (d) air-sea temperature difference (air temperature at 10 m − SST) temporal variability are spatially averaged over the domain and over the same time period in which α and β are obtained. (e) correlation between wind speed and α with Pearson correlation coefficient r_{W_α}. (f) correlation between wind speed and β with Pearson correlation coefficient r_{W_β}. (g) correlation between air-sea temperature difference and β with Pearson correlation coefficient r_{T_β}.

illustrated by the distribution of wind stress curl as a function of surface vorticity and crosswind SST gradient (Fig. 2). Incorporation of both feedbacks improves the skill of hourly wind stress field estimations compared with the traditional (univariate 1D) approaches (Fig. 3). These relationships are summarized in terms of coefficients α and β that describe the dependence on vorticity and crosswind SST gradients, respectively. The coefficient fluctuations are highly correlated with variations in domain-averaged wind speed and air-sea temperature difference, respectively. In this section, we discuss implications of these small-scale wind-front interactions (Fig. 2) as well as some limitations of the linear reconstruction.

The TFB and CFB have been shown to interfere with each other and together modify the wind stress fields, yet the interaction between them seem to remain largely linear, from larger mesoscale scales, $O(100)$ km, to the resolved sub-mesoscale scales in this study, $O(10)$ km. This is substantiated through comparing the accuracy of various wind stress curl reconstructions in Fig. 3. First, wind stress curl reconstructions are similar using either a 2D dependent sum or 1D independent sum. Yet, using TFB or CFB alone leads to a larger domain-averaged RMSE, up to 60% and 190%, respectively. This suggests that, at sub-mesoscales, reconstruction of the wind stress curl based on both feedbacks is more accurate than using either one feedback, given that the feedback dominance can vary with time. The 2D dependent sum does not significantly outperform the 1D independent sum. Ocean vorticity and crosswind SST gradients are therefore largely independent at $\sim$10 km. The accuracy of 1D independent sum is likely to deteriorate as the model resolution increases, allowing for stronger, non-linear fronts.

While consideration of both vorticity and SST gradients improves wind stress curl reconstruction over 1D individual estimates, there remain periods when the inferred wind stress curl field differs significantly from the simulated output, at least as measured by r^2 (Fig. 3). Further analysis of the reconstructed snapshots during these periods as well as the RMSE suggests a more nuanced relationship. During high r^2 events ($r^2 > 0.6$), the simulated wind stress curl is dominated by vorticity and strain structures that reflect those at the ocean surface. In most of the anomalously low r^2 events ($r^2 < 0.2$), the simulation is characterized by a large-scale, anomalous wind stress curl event that obscures the underlying fine-scale structures, which is potentially related to synoptic storms. The proposed 2D coefficients support reconstruction of the slowly-varying wind stress curl structures, therefore leading to occasional low r^2 values when synoptic transient events dominate the wind field. Indeed, removing the domain averaged wind stress derivatives at those instances recovers some finescale structures and raises r^2 by 25-50%.

Spatially, the coefficients of the CFB and TFB are not uniform throughout the domain, but are instead tied to coherent structures, such as filamentary strain or eddy vorticity centers determined by the Okubo-Weiss parameter (SI). This information may be useful for future observational campaigns, such as Sub-Mesoscale Ocean Dynamics Experiment (S-MODE) (Farrar et al., 2020), both in terms of experiment design and real-time adaptive sampling.The different characteristic time scales of variability for α and β, as well as the correlation and spread between the two coefficients and physical properties, suggest that the feedbacks vary in response to different physical processes. Vorticity coefficients α are linearly correlated with wind stress magnitude ($r_{W_\alpha} > 0.8$) for all three time windows (Fig. 4 e), indicating an almost instantaneous domain-wide adjustment to wind stress curl through changes in relative velocities. The TFB coefficient β correlates with both air-sea temperature difference and wind speed, yet the spread is almost twice as large in the wind speed correlation. Since the highest r_{T_β} occurs at daily time scales (Fig. 4 g), we infer that air-sea temperature differences and the daily atmospheric heating/cooling cycle explain most of the variance for high frequency variations of β. This is consistent with Desbiolles et al. (2023), which identified a correlation at daily time scale between 1D thermal feedback and air-sea temperature gradients in reanalysis data. In contrast, r_{W_β} remains moderate for all time scales. The larger spread may

be explained by a longer time for wind speed adjustment through downward momentum mixing in the atmospheric boundary layer as compared to air-sea temperature thermal adjustments. A more detailed mechanistic analysis of β and its relationship to wind speed and air-sea temperature gradient is needed.

This study has focused on simulated, wintertime properties from Drake Passage, Southern Ocean. This region hosts especially vigorous mesoscale and sub-mesoscale flow fields (Luecke et al., 2017), enabling strong wind-front interactions and the potential for enhanced ventilation. Compared to the rest of the global ocean, properties unique to the Southern Ocean include stronger surface winds (Flexas et al., 2019) (Fig. 1 b), sharper surface density gradients, deeper mixed layers (Dong et al., 2008), and weaker stratification, which, combined with the connectedness to the world ocean basins (Talley, 2013), make the Southern Ocean a critical location where the impact of wind-front interactions and modifications to air-sea fluxes may have a global impact (Nicholson et al., 2022). The stronger sub-mesoscale modification to wind stress curl in this study, through Ekman dynamics (Gaube et al., 2015; Seo et al., 2016), might potentially enhance vertical velocities in the upper ocean. The impact on transport of tracers, ventilation, and stratification in the surface mixed layer is a topic worth exploring in future studies (Morrison et al., 2022; Swart et al., 2023).

5 Conclusion

Estimation of both the structure and magnitude of wind stress curl or divergence improves when the combined impact of surface ocean velocity and SST gradients, or the synergy of current and thermal feedbacks, are considered. Conditional mean plots of wind stress curl and wind stress divergence illustrate that in the Southern Ocean, the two feedback constructively and destructively interact and jointly control anomalies in the wind fields at sub-mesoscale. Temporal variability of each feedback is tied to physical properties such as wind speed or air-sea temperature difference, or both, implying the underlying mechanical and thermodynamical mechanisms of wind-front interactions. The results presented in this study are based on an energetic domain that is relevant to other strong western boundary currents. Yet, the mechanism of wind-front interactions is generic and applies to other ocean regions with varied intensity. A more comprehensive quantification of the two feedbacks is indispensable to constrain the calculation of air-sea fluxes and ocean surface properties. This study highlights the need for future observational endeavors with collocated measurements of surface currents, SST, and surface wind stress.

Acknowledgments

YB acknowledges support from the National Aeronautics and Space Administration Science Mission Directorate FINESST program under Award No. 80NSSC21K1635. AFT and ABVB were supported by NASA grant 80NSSC19K1004; ABVB received additional support from the NSF award OCE-2241822.

Open Research

The coupled ocean-atmosphere simulation used in this study is accessible through: (a) any NASA Ames Supercomputer at ∼ dmenemen/c1440_llc2160; (b) xmitgcm: `https://xmitgcm.readthedocs.io`; (c) NASA Ames data portal: `https://data.nas.nasa.gov/ecco/data.php`.

References

Balwada, D., Smith, K. S., & Abernathey, R. (2018). Submesoscale vertical velocities enhance tracer subduction in an idealized antarctic circumpolar current.

Geophysical Research Letters, *45*(18), 9790–9802.

Barkan, R., Molemaker, M. J., Srinivasan, K., McWilliams, J. C., & D'Asaro, E. A. (2019). The role of horizontal divergence in submesoscale frontogenesis. *Journal of Physical Oceanography*, *49*(6), 1593–1618.

Buckingham, C. E., Naveira Garabato, A. C., Thompson, A. F., Brannigan, L., Lazar, A., Marshall, D. P., ... Belcher, S. E. (2016). Seasonality of submesoscale flows in the ocean surface boundary layer. *Geophysical Research Letters*, *43*(5), 2118–2126.

Bye, J. A. (1985). Large-scale momentum exchange in the coupled atmosphere-ocean. In *Elsevier oceanography series* (Vol. 40, pp. 51–61). Elsevier.

Callies, J., Barkan, R., & Naveira Garabato, A. (2020). Time scales of submesoscale flow inferred from a mooring array. *Journal of Physical Oceanography*, *50*(4), 1065–1086.

Chang, P., Zhang, S., Danabasoglu, G., Yeager, S. G., Fu, H., Wang, H., ... Fu, L., Dan andWu (2020). An unprecedented set of high-resolution earth system simulations for understanding multiscale interactions in climate variability and change. *Journal of Advances in Modeling Earth Systems*, *12*(12), e2020MS002298.

Chelton, D. B., Esbensen, S. K., Schlax, M. G., Thum, N., Freilich, M. H., Wentz, F. J., ... Schopf, P. S. (2001). Observations of coupling between surface wind stress and sea surface temperature in the eastern tropical pacific. *Journal of Climate*, *14*(7), 1479–1498.

Chelton, D. B., Schlax, M. G., Freilich, M. H., & Milliff, R. F. (2004). Satellite measurements reveal persistent small-scale features in ocean winds. *science*, *303*(5660), 978–983.

Chelton, D. B., Schlax, M. G., & Samelson, R. M. (2007). Summertime coupling between sea surface temperature and wind stress in the california current system. *Journal of Physical Oceanography*, *37*(3), 495–517.

Chelton, D. B., Schlax, M. G., & Samelson, R. M. (2011). Global observations of nonlinear mesoscale eddies. *Progress in oceanography*, *91*(2), 167–216.

Chelton, D. B., & Xie, S.-P. (2010). Coupled ocean-atmosphere interaction at oceanic mesoscales. *Oceanography*, *23*(4), 52–69.

Chen, X., Dewar, W., Chassignet, E., Bourassa, M., Morey, S., & Gopalakrishnan, G. (2022). On the feedback between air-sea turbulent momentum flux and oceanic submesoscale processes. *Journal of Geophysical Research: Oceans*, *127*(10), e2022JC018767.

Desbiolles, F., Meroni, A. N., Renault, L., & Pasquero, C. (2023). Environmental control of wind response to sea surface temperature patterns in reanalysis dataset. *Journal of Climate*, 1–31.

Dong, S., Sprintall, J., Gille, S. T., & Talley, L. (2008). Southern ocean mixed-layer depth from argo float profiles. *Journal of Geophysical Research: Oceans*, *113*(C6).

Dove, L. A., Balwada, D., Thompson, A. F., & Gray, A. R. (2022). Enhanced ventilation in energetic regions of the antarctic circumpolar current. *Geophysical Research Letters*, *49*(13), e2021GL097574.

Dove, L. A., Thompson, A. F., Balwada, D., & Gray, A. R. (2021). Observational evidence of ventilation hotspots in the southern ocean. *Journal of Geophysical Research: Oceans*, *126*(7), e2021JC017178.

Dove, L. A., Viglione, G. A., Thompson, A. F., Flexas, M. M., Cason, T. R., & Sprintall, J. (2023). Controls on wintertime ventilation in southern drake passage. *Geophysical Research Letters*, *50*(5), e2022GL102550.

Farrar, J. T., D'Asaro, E., Rodriguez, E., Shcherbina, A., Czech, E., Matthias, P., ... Jenkins, R. (2020). S-mode: The sub-mesoscale ocean dynamics experiment. In *Igarss 2020-2020 ieee international geoscience and remote sensing symposium* (pp. 3533–3536).

Flexas, M. M., Thompson, A. F., Torres, H. S., Klein, P., Farrar, J. T., Zhang, H., & Menemenlis, D. (2019). Global estimates of the energy transfer from the wind to the ocean, with emphasis on near-inertial oscillations. *Journal of Geophysical Research: Oceans*, *124*(8), 5723–5746.

Foussard, A., Lapeyre, G., & Plougonven, R. (2019). Storm track response to oceanic eddies in idealized atmospheric simulations. *Journal of Climate*, *32*(2), 445–463.

Frenger, I., Gruber, N., Knutti, R., & Münnich, M. (2013). Imprint of southern ocean eddies on winds, clouds and rainfall. *Nature geoscience*, *6*(8), 608–612.

Gaube, P., Chelton, D. B., Samelson, R. M., Schlax, M. G., & O'Neill, L. W. (2015). Satellite observations of mesoscale eddy-induced ekman pumping. *Journal of Physical Oceanography*, *45*(1), 104–132.

Gruber, N., Landschützer, P., & Lovenduski, N. S. (2019). The variable southern ocean carbon sink. *Annual review of marine science*, *11*, 159–186.

Hoskins, B. J., & Brertherton, F. P. (1972). Atmospheric frontogenesis models: mathematical formulation and solution. *Journal of the Atmospheric Sciences*, *295*.

Luecke, C., Arbic, B., Bassette, S., Richman, J., Shriver, J., Alford, M., ... Wallcraft, A. (2017). The global mesoscale eddy available potential energy field in models and observations. *Journal of Geophysical Research: Oceans*, *122*(11), 9126–9143.

Marshall, J., & Speer, K. (2012). Closure of the meridional overturning circulation through southern ocean upwelling. *Nature geoscience*, *5*(3), 171–180.

McWilliams, J. C. (2016). Submesoscale currents in the ocean. *Proceedings of the Royal Society A: Mathematical, Physical and Engineering Sciences*, *472*(2189), 20160117.

Morrison, A. K., Waugh, D. W., Hogg, A. M., Jones, D. C., & Abernathey, R. P. (2022). Ventilation of the southern ocean pycnocline. *Annual Review of Marine Science*, *14*, 405–430.

Nicholson, S. A., Whitt, D. B., Fer, I., du Plessis, M. D., Lebéhot, A. D., Swart, S., ... Monteiro, P. M. (2022). Storms drive outgassing of CO2 in the subpolar southern ocean. *Nature communications*, *13*(1), 158.

O'Neill, L. W., Chelton, D. B., & Esbensen, S. K. (2012). Covariability of surface wind and stress responses to sea surface temperature fronts. *Journal of Climate*, *25*(17), 5916–5942.

Rai, S., Hecht, M., Maltrud, M., & Aluie, H. (2021). Scale of oceanic eddy killing by wind from global satellite observations. *Science Advances*, *7*(28), eabf4920.

Renault, L., Masson, S., Oerder, V., Colas, F., & McWilliams, J. C. (2023). Modulation of the oceanic mesoscale activity by the mesoscale thermal feedback to the atmosphere. *Journal of Physical Oceanography*.

Renault, L., Masson, S., Oerder, V., Jullien, S., & Colas, F. (2019). Disentangling the mesoscale ocean-atmosphere interactions. *Journal of Geophysical Research: Oceans*, *124*(3), 2164–2178.

Renault, L., McWilliams, J. C., & Gula, J. (2018). Dampening of submesoscale currents by air-sea stress coupling in the californian upwelling system. *Scientific reports*, *8*(1), 1–8.

Renault, L., McWilliams, J. C., & Masson, S. (2017). Satellite observations of imprint of oceanic current on wind stress by air-sea coupling. *Scientific reports*, *7*(1), 1–7.

Renault, L., Molemaker, M. J., McWilliams, J. C., Shchepetkin, A. F., Lemarié, F., Chelton, D., ... Hall, A. (2016). Modulation of wind work by oceanic current interaction with the atmosphere. *Journal of Physical Oceanography*, *46*(6), 1685–1704.

Rooth, C., & Xie, L. (1992). Air-sea boundary layer dynamics in the presence of mesoscale surface currents. *Journal of Geophysical Research: Oceans*, *97*(C9),

14431–14438.

Seo, H., Miller, A. J., & Norris, J. R. (2016). Eddy–wind interaction in the california current system: Dynamics and impacts. *Journal of Physical Oceanography*, *46*(2), 439–459.

Seo, H., O'Neill, L. W., Bourassa, M. A., Czaja, A., Drushka, K., Edson, J. B., ... Qing, W. (2023). Ocean mesoscale and frontal-scale ocean–atmosphere interactions and influence on large-scale climate: A review. *Journal of Climate*, *36*(7), 1981–2013.

Siegelman, L., Klein, P., Rivière, P., Thompson, A. F., Torres, H. S., Flexas, M. M., & Menemenlis, D. (2020). Enhanced upward heat transport at deep submesoscale ocean fronts. *Nature Geoscience*, *13*(1), 50–55.

Small, R. J., Bryan, F. O., Bishop, S. P., & Tomas, R. A. (2019). Air–sea turbulent heat fluxes in climate models and observational analyses: What drives their variability? *Journal of Climate*, *32*(8), 2397–2421.

Small, R. J., deSzoeke, S. P., Xie, S., O'Neill, L., Seo, H., Song, Q., ... Minobe, S. (2008). Air–sea interaction over ocean fronts and eddies. *Dynamics of Atmospheres and Oceans*, *45*(3-4), 274–319.

Strobach, E., Klein, P., Molod, A., Fahad, A. A., Trayanov, A., Menemenlis, D., & Torres, H. (2022). Local air-sea interactions at ocean mesoscale and submesoscale in a western boundary current. *Geophysical Research Letters*, *49*(7), e2021GL097003.

Swart, S., du Plessis, M. D., Nicholson, S. A., Monteiro, P. M. S., Dove, L. A., Thomalla, S., ... de Souza, R. B. (2023). The southern ocean mixed layer and its boundary fluxes: fine-scale observational progress and future research priorities. *Phil. Trans. R. Soc. A.*, *381*.

Takatama, K., & Schneider, N. (2017). The role of back pressure in the atmospheric response to surface stress induced by the kuroshio. *Journal of the Atmospheric Sciences*, *74*(2), 597–615.

Talley, L. D. (2013). Closure of the global overturning circulation through the indian, pacific, and southern oceans: Schematics and transports. *Oceanography*, *26*(1), 80–97.

Taylor, J. R., & Thompson, A. F. (2023). Submesoscale dynamics in the upper ocean. *Annual Review of Fluid Mechanics*, *55*.

Thomas, L. N., Tandon, A., & Mahadevan, A. (2008). Submesoscale processes and dynamics. *Ocean Modeling in an Eddying Regime, Geophysical Monograph Series*, *177*, 17–38.

Torres, H. S., Klein, P., Wang, J., Wineteer, A., Qiu, B., Thompson, A. F., ... Perkovic-Martin, D. (2022). Wind work at the air-sea interface: a modeling study in anticipation of future space missions. *Geoscientific Model Development*, *15*(21), 8041–8058.

Xu, Y., & Scott, R. B. (2008). Subtleties in forcing eddy resolving ocean models with satellite wind data. *Ocean Modelling*, *20*(3), 240–251.

Figure.

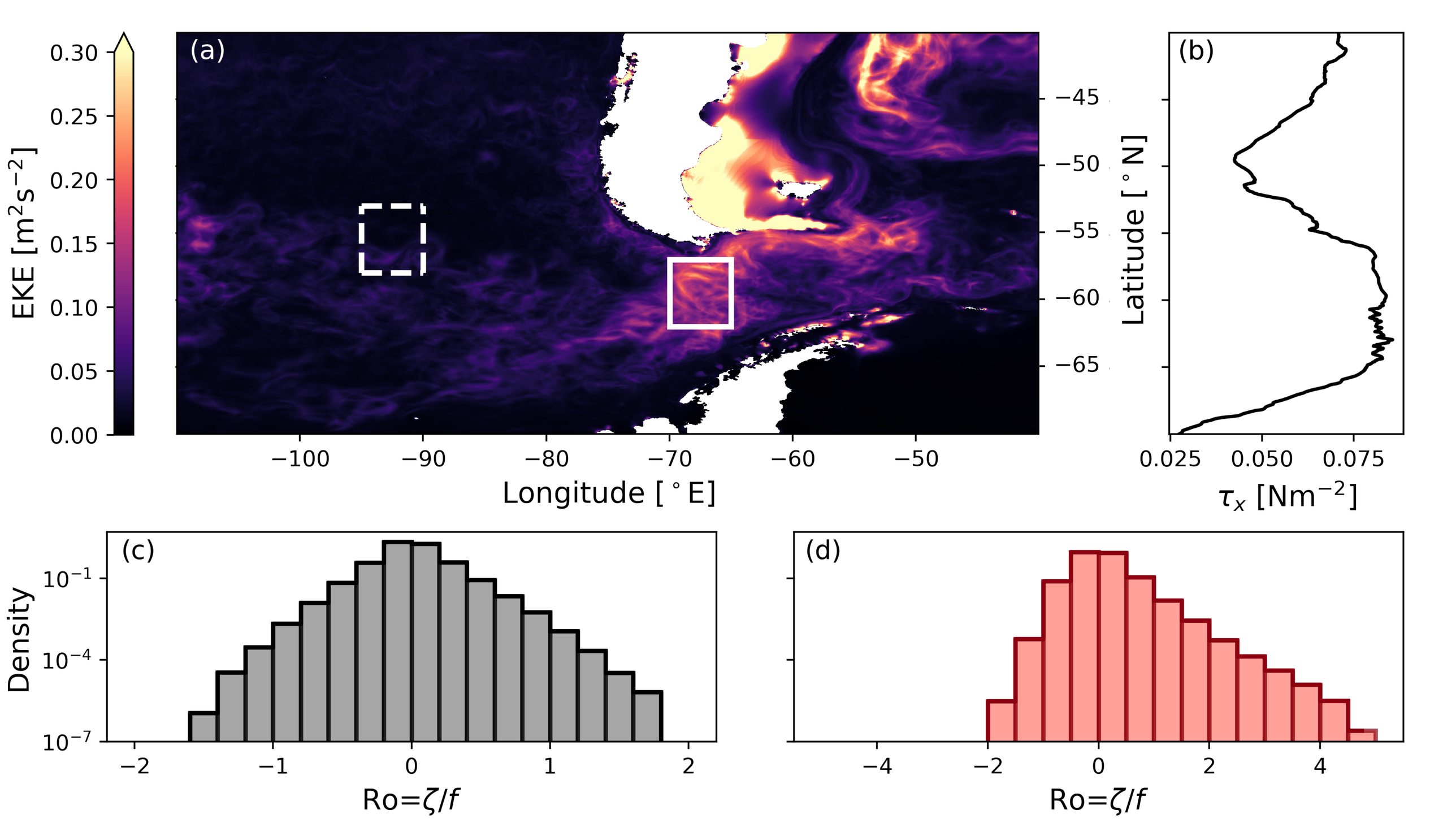
(a)
(b)
(c)
(d)
EKE [m^{2}s^{-2}]
0.30
0.25
0.20
0.15
0.10
0.05
0.00
−100
−90
−80
−70
−60
−50
Longitude [˚E]
−45
−50
−55
−60
−65
Latitude [˚N]
0.025
0.050
0.075
τ_x [Nm^{-2}]
Density
10^{-1}
10^{-4}
10^{-7}
−2
−1
0
1
2
Ro=ζ/f
−4
−2
0
2
4
Ro=ζ/f

Figure.

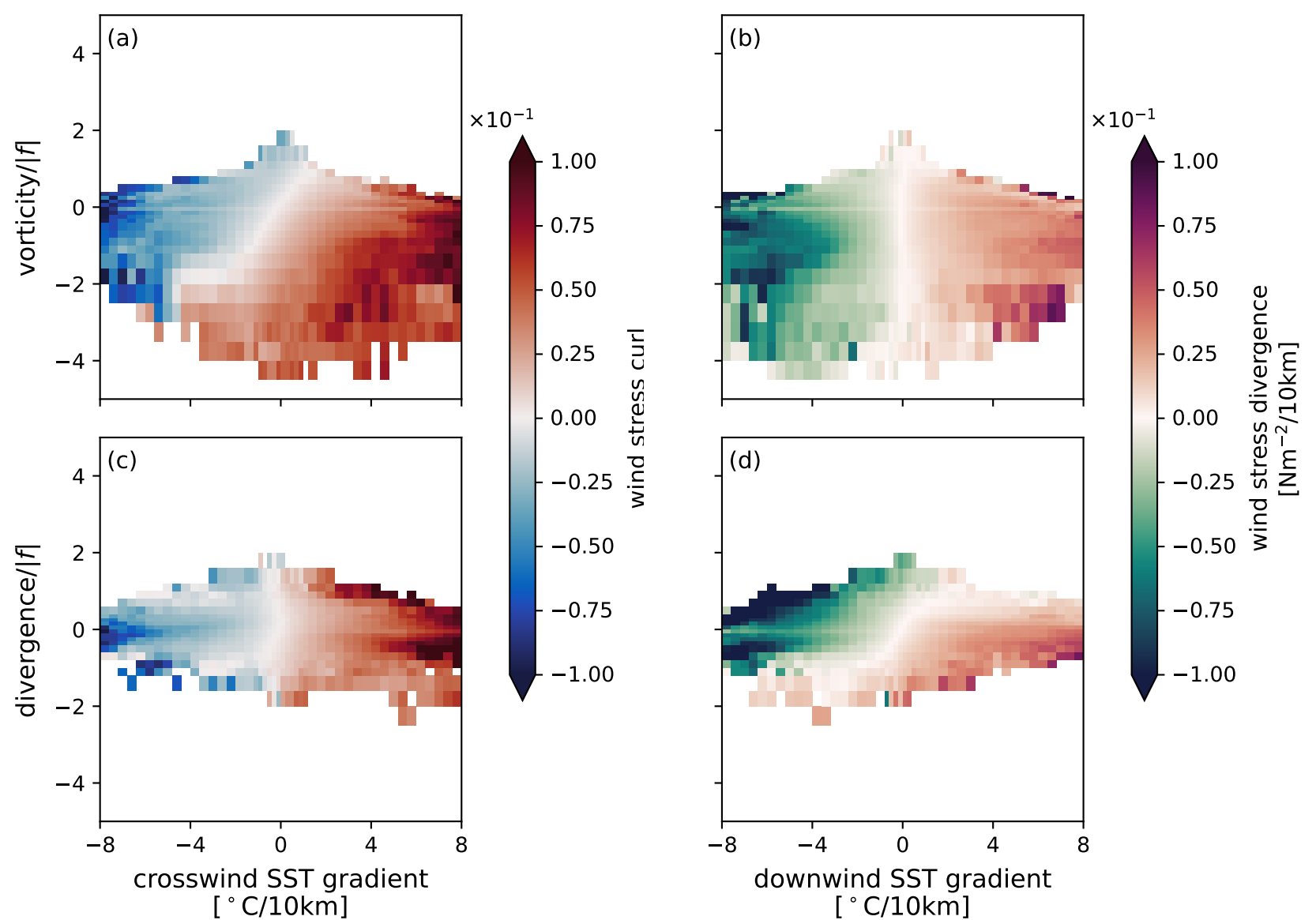
(a)
(b)
(c)
(d)
vorticity/|f|
divergence/|f|
×10⁻¹
wind stress curl
wind stress divergence
[Nm⁻²/10km]
crosswind SST gradient
[°C/10km]
downwind SST gradient
[°C/10km]
4
2
0
−2
−4
−8
−4
0
4
8
1.00
0.75
0.50
0.25
0.00
−0.25
−0.50
−0.75
−1.00

Figure.

(a) (b) (c) (d) (e)

(f) (g) (h) (i) (j)

Latitude [° N]

Longitude [° E]

wind stress curl [Nm^{-2}/10km]

(k)

2-D
1-D current+thermal
1-D current
1-D thermal
top panel
middle panel

r^2 of reconstruction

(l)

1-D RMSEs / 2-D RMSE

time [hr]

Figure.

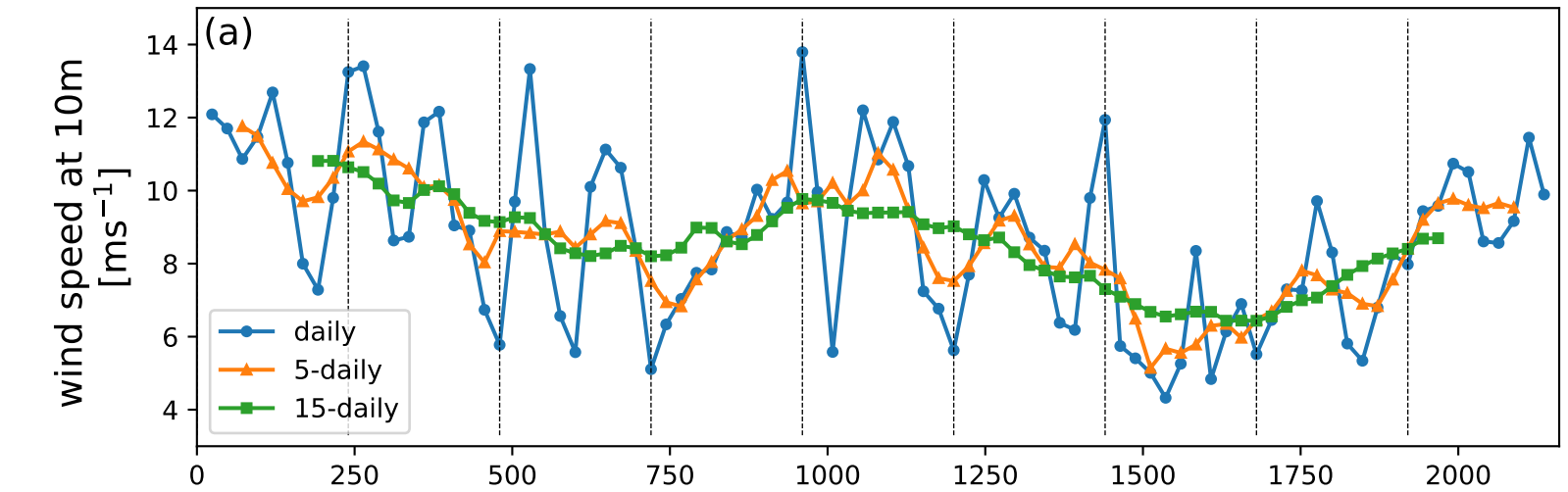
(a)
wind speed at 10m [ms^{-1}]
daily
5-daily
15-daily

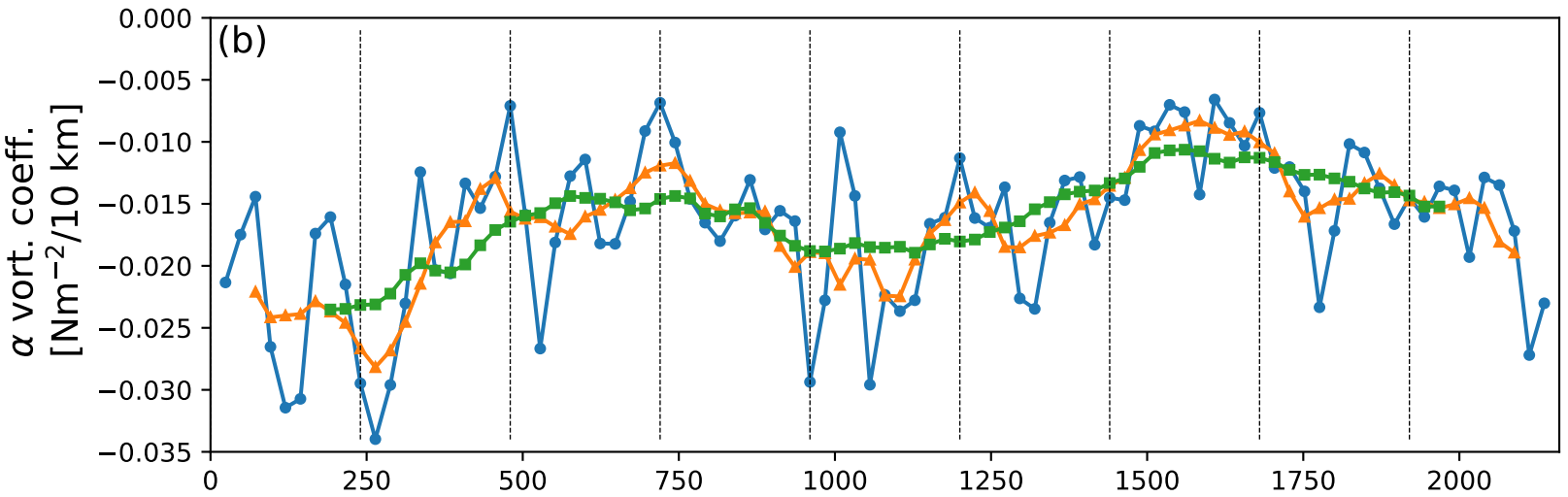
(b)
α vort. coeff. [Nm^{-2}/10 km]

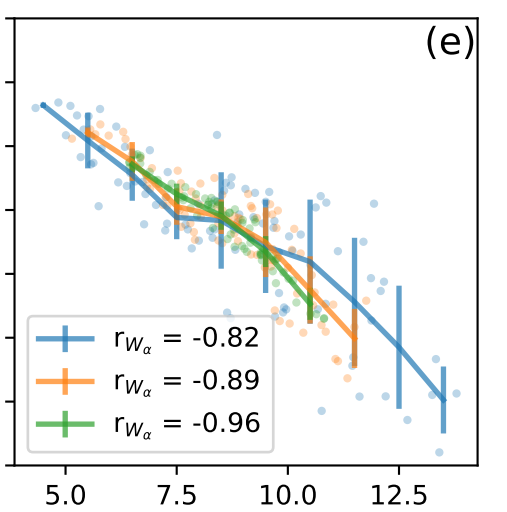
(e)
r_{W_α} = -0.82
r_{W_α} = -0.89
r_{W_α} = -0.96

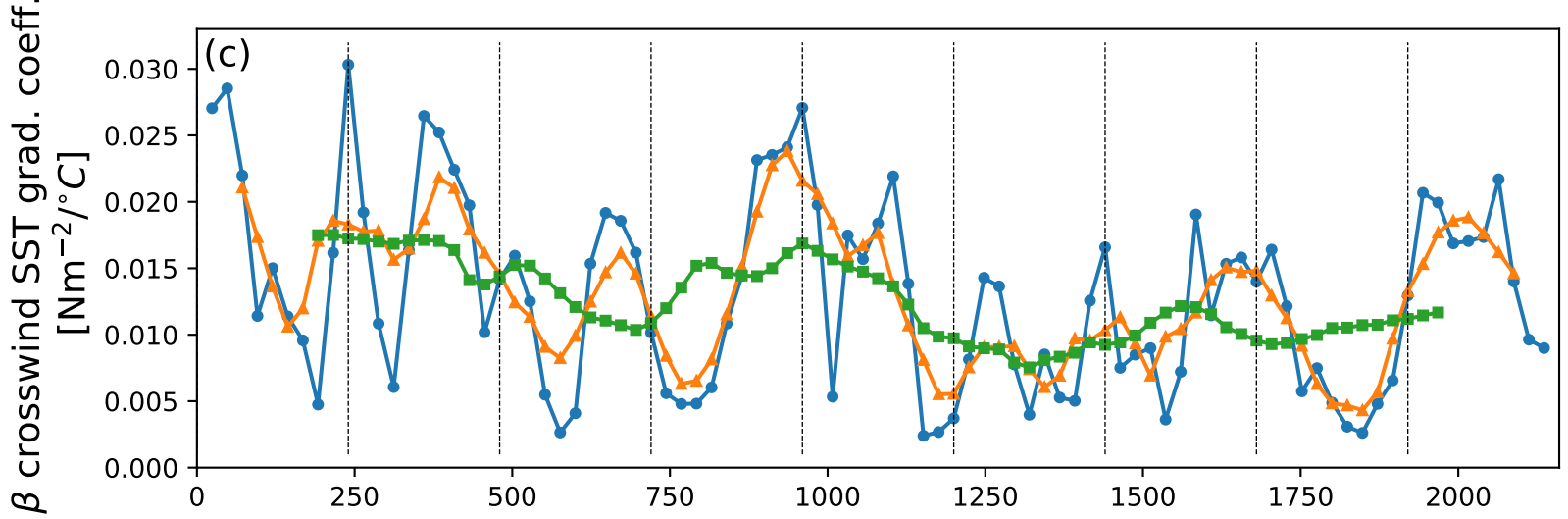
(c)
β crosswind SST grad. coeff. [Nm^{-2}/$^\circ$C]

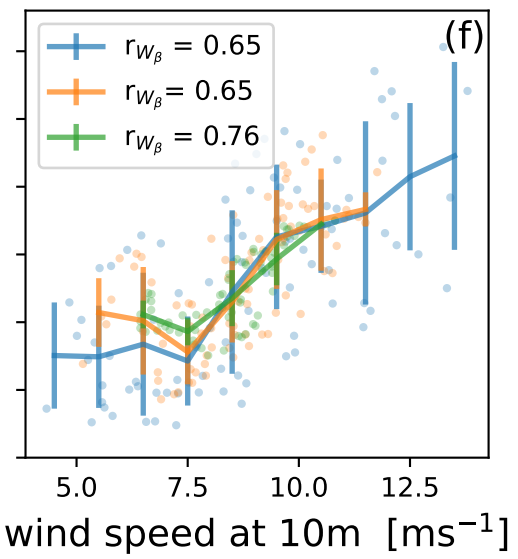
(f)
r_{W_β} = 0.65
r_{W_β}= 0.65
r_{W_β} = 0.76
wind speed at 10m [ms^{-1}]

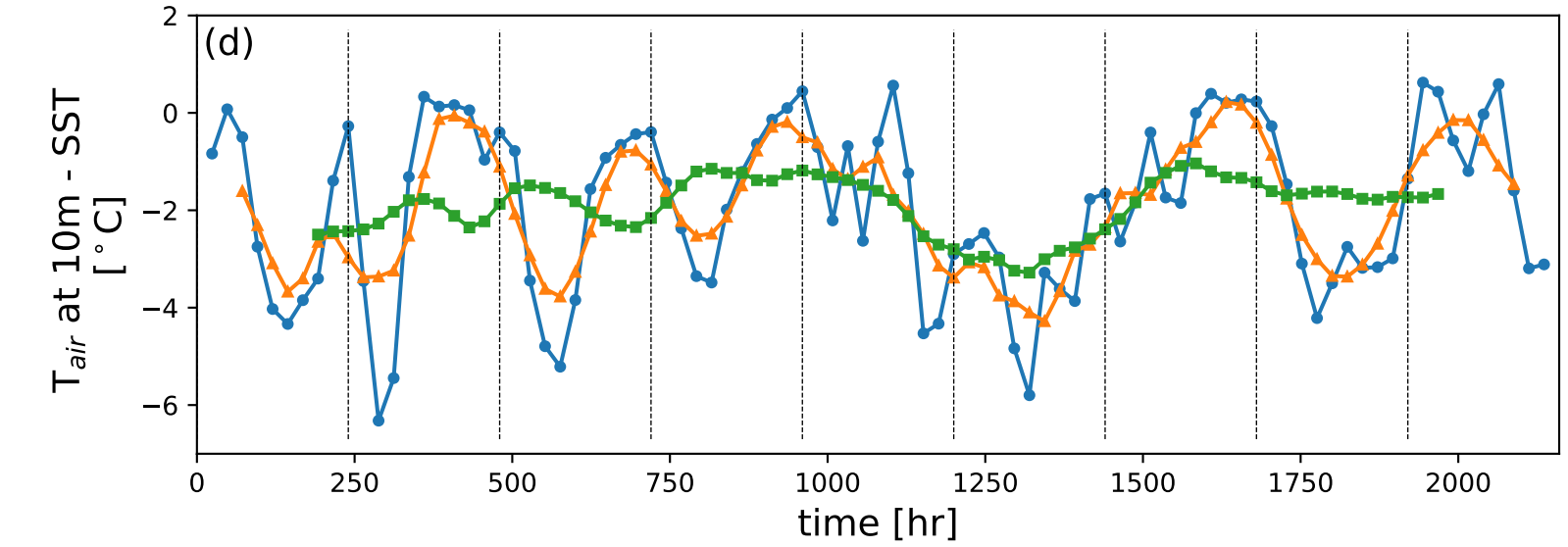
(d)
T_{air} at 10m - SST [$^\circ$C]
time [hr]

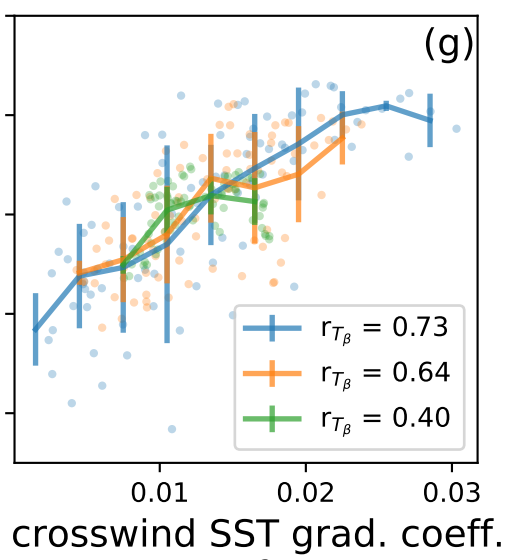
(g)
r_{T_β} = 0.73
r_{T_β} = 0.64
r_{T_β} = 0.40
β crosswind SST grad. coeff. [Nm^{-2}/$^\circ$C]